Journal of Volcanology and Geothermal Research 289 (2014) 202–209

Contents lists available at ScienceDirect

Journal of Volcanology and Geothermal Research

journal homepage: www.elsevier.com/locate/jvolgeores

Conditions and timescales for welding block-and-ash flow deposits

M.J. Heap [a,b,*], S. Kolzenburg [a], J.K. Russell [a], M.E. Campbell [a], J. Welles [a], J.I. Farquharson [b], A. Ryan [a]

[a] Volcanology and Petrology Laboratory, Department of Earth and Ocean Sciences, University of British Columbia, Vancouver, V6T 1Z4, Canada
[b] Laboratoire de Déformation des Roches, Équipe de Géophysique Expérimentale, Institut de Physique de Globe de Strasbourg (UMR 7516 CNRS, Université de Strasbourg/EOST), 5 rue René Descartes, 67084 Strasbourg cedex, France

ARTICLE INFO

Article history:
Received 21 August 2014
Accepted 23 November 2014
Available online 5 December 2014

Keywords:
Sintering
Compaction
Viscosity
Porosity
Permeability
Mount Meager

ABSTRACT

Welding of pyroclastic deposits to reform a coherent rock mass is a common phenomenon, especially for pumiceous pyroclastic density current deposits (i.e., ignimbrites). However, and despite the pervasive abundance of block-and-ash flow (BAF) deposits in the geological and modern record, instances of strongly welded BAF deposits are few. Here, we present a series of high-temperature (800-900 °C) compaction experiments designed to map the conditions (deposit thickness/stress and temperature/viscosity) and timescales that permit or inhibit the welding of BAF deposits. Our experiments were performed on unconsolidated aggregates (containing an ash and lapilli component) derived from crushed and sieved lava blocks (containing 25% crystals) taken from the well-documented welded BAF deposit at Mount Meager volcano (British Columbia, Canada). The experiments demonstrate that welding efficiency increases with increasing time and temperature. Progressive welding is expressed by increasing axial strain, porosity loss, and bulk density. The rate of change of each of these physical properties reduces as welding progresses. Microstructural analysis of the experimental products shows that the loss of interclast porosity during welding results from the progressive sintering and amalgamation of vitric fragments, and that the pore shape changes from sub-equant pores to stretched lenses sandwiched between vitric and crystal fragments. The coincidence between the microstructure and rock physical properties of the natural and experimental samples highlight that we have successfully reproduced welded BAF in the laboratory. Furthermore, our permeability measurements highlight a hysteresis in the return journey of the "*there-and-back-again*" volcanic permeability cycle (expressed by an increase in permeability due to vesiculation and fragmentation followed by a decrease due to welding). This hysteresis cannot be described by a single porosity-permeability power law relationship and reflects the change in pore shape and connectivity during welding. Finally, we show that a simple model for welding can accurately forecast the welding timescales of the BAF deposit at Mount Meager (as reconstructed from the collapse of the Lillooet River valley dam) using our experimental data. We use this validation as a platform to provide a universal window for the welding of BAF deposits, also applicable for comparable welded deposits (e.g., welded autobreccias in block-lavas and lava domes), for a broad range of deposit thickness (or stress) and effective viscosity.

1. Introduction

The explosive or gravitational collapse of silicic lavas or lava domes commonly generate pyroclastic density currents characterised by a large fraction of dense (non-pumiceous) juvenile blocks and lapilli supported by an ash matrix. This type of pyroclastic flow is termed a "block-and-ash flow" (BAF). BAFs are common products of effusive to explosive volcanism at many intermediate to felsic stratovolcanoes, such as Unzen (Japan; e.g., Ui et al., 1999), Merapi (Indonesia; e.g., Abdurachman et al., 2000), Soufriére Hills volcano (Montserrat; e.g., Cole et al., 2002), Mt Pelée (Martinique; e.g., Fisher and Heiken, 1982), and Volcán de Colima (Mexico; e.g., Rodríguez-Elizarrarás et al., 1991), and pose a substantial economic and humanitarian threat.

Pyroclastic deposits can weld to form a coherent rock mass if emplaced above the glass transition temperature (Tg) of their melt phase (e.g., Guest and Rogers, 1967; Grunder and Russell, 2005; Giordano et al., 2008). The observation of welding (the viscous sintering and amalgamation of vitric fragments) is most common within pumice-rich pyroclastic deposits (e.g., Wright and Cashman, 2013); the high volume fraction of vitric, vesicular juvenile pyroclasts (e.g., pumice and vitric shards) are highly susceptible to viscous sintering for as long as they reside above Tg. By contrast, the source materials for BAFs (lavas and domes) are commonly more crystalline, more outgassed (i.e., less porous), and closer to the Tg of their melt phase. Consequently, documented examples of welded BAF deposits are relatively rare (e.g., see Cas and Wright, 1987). To date, and for this reason,

* Corresponding author at: Laboratoire de Déformation des Roches, Équipe de Géophysique Expérimentale, Institut de Physique de Globe de Strasbourg (UMR 7516 CNRS, Université de Strasbourg/EOST), 5 rue René Descartes, 67084 Strasbourg cedex, France.
E-mail address: heap@unistra.fr (M.J. Heap).

http://dx.doi.org/10.1016/j.jvolgeores.2014.11.010
0377-0273/

experimental welding studies within a volcanological context have focussed on pumiceous vitric materials containing no crystal cargo (e.g., Friedman et al., 1963; Bierwirth, 1982; Grunder et al., 2005; Quane and Russell, 2005; Quane et al., 2009; Vasseur et al., 2013). The first order results, and models, from these studies need not be (or are unlikely to be) applicable to welding processes in crystal-bearing deposits. Further, theoretical analyses often consider crystal-bearing or bubble-bearing magmas separately, due to the complexity of three-phase magmatic/volcanic systems (Mader et al., 2013).

Mount Meager is a Quaternary volcano located in southwest British Columbia, Canada and is part of the Garibaldi Volcanic Belt, the northernmost segment of the Cascade Volcanic Belt. The 2360 B.P. eruption of Mount Meager is the youngest explosive volcanic eruption in Canada; it is relevant to this study because the waning stages of the eruption produced a thick (>160 m) succession of BAF deposits that filled and dammed the Lillooet River valley forming an ephemeral lake (Hickson et al., 1999; Michol et al., 2008; Andrews et al., 2014). A significant portion of these BAF deposits are densely-welded (Fig. 1A and 1B) and are currently exposed in a 100 m rock wall resulting from collapse of the pyroclastic dam and erosion by the concomitant flood (Fig. 1A, Hickson et al., 1999; Michol et al., 2008; Andrews et al., 2014). Other examples of welded BAF deposits may exist in the Arico Ignimbrite in Tenerife, Spain (Rodríguez-Losada et al., 2007 and references therein), in the pyroclastic deposits of the 1783 eruption of Asama volcano, Japan (Yasui and Koyaguchi, 2004), in Marysvale, Utah, U.S.A (Kerr et al., 1974), and in the San Juan volcanic field, Colorado, U.S.A. (Bachmann et al., 2000).

The well-exposed deposits at Mount Meager volcano provide the opportunity to study variably-welded BAF deposits. Here, we present an experimental study designed to investigate the conditions and timescales required to weld the pyroclastic BAF materials at Mount Meager volcano. We then compare the experimental products with the natural welded deposit, and use the experimental data to map out the conditions (thickness/stress and effective viscosity) and timescales required to weld BAF deposits (and other comparable welded deposits; e.g., welded autobreccias in block-lavas and lava domes).

2. Materials and methods

2.1. Materials

We collected the fresh (non-oxidised), most glassy blocks (approximately 30 cm x 30 cm x 30 cm) from the poorly (incipiently) welded facies of BAF deposits preserved at Mount Meager volcano to prepare our samples. We anticipate that this material best represents the original juvenile dome lava. The average bulk density and total porosity of the lava are 2380 kg/m^3 and 5%, respectively. Optical microscopic analysis yielded an average crystal content of about 25%, and chemical analysis of the glass phase (Stewart, 2002) is consistent with a calculated Tg between 550 and 700 °C, depending on dissolved magmatic water content (Giordano et al., 2008). The collected lava blocks were either powdered or crushed. We then sieved the aggregate material into four size fractions: fine ash (<< 2 mm), ash (<2 mm), very fine lapilli (2-4 mm), and fine lapilli (4-8 mm). The sample material used in our experiments was an aggregate comprising 60% ash (40% fine ash, and 20% ash) and 40% lapilli (30% very fine lapilli, and 10% fine lapilli) sized particles. Laser particle size distribution analysis (Fig. 2) shows that the ash component mainly comprises ash particles between 100 and 2000 μm, and that the most common particle size is 1000 μm. The fine ash component contains many more particles below 100 μm and exhibits a bimodal particle size distribution with peaks at 100 and 700 μm. The aggregates were homogenised and poured into ceramic sleeves (3.5 mm thick, with an internal diameter of 41 mm) and contained between 5 mm thick precision-ground ceramic spacers, three at the bottom of the sample and one at the top. Each sample contained exactly 176 g of the ash and lapilli mixture, which resulted in a sample height between 80 and 85 mm. We take the porosity of the starting material as the interclast porosity (calculated using 2497 kg/m^3 for the powder skeletal density of the lava) at an axial stress of 0.03 MPa (to ensure similar aggregate packing); the average porosity of our experimental aggregates was 35% (Table 1). While we appreciate that a minor intraclast porosity component to the lapilli fragments is probable (the lava contains a total porosity of 5%), we ignore this small contribution to the starting porosity of our aggregate samples. We also note that, during the experiments, the sample porosity is occupied by air; during welding of the natural deposits, pore space is probably filled with a mixture of air and magmatic volatiles allowing for volatile resorption into the glassy fragments that could assist welding (e.g., Sparks et al., 1999; Ryan et al., 2014).

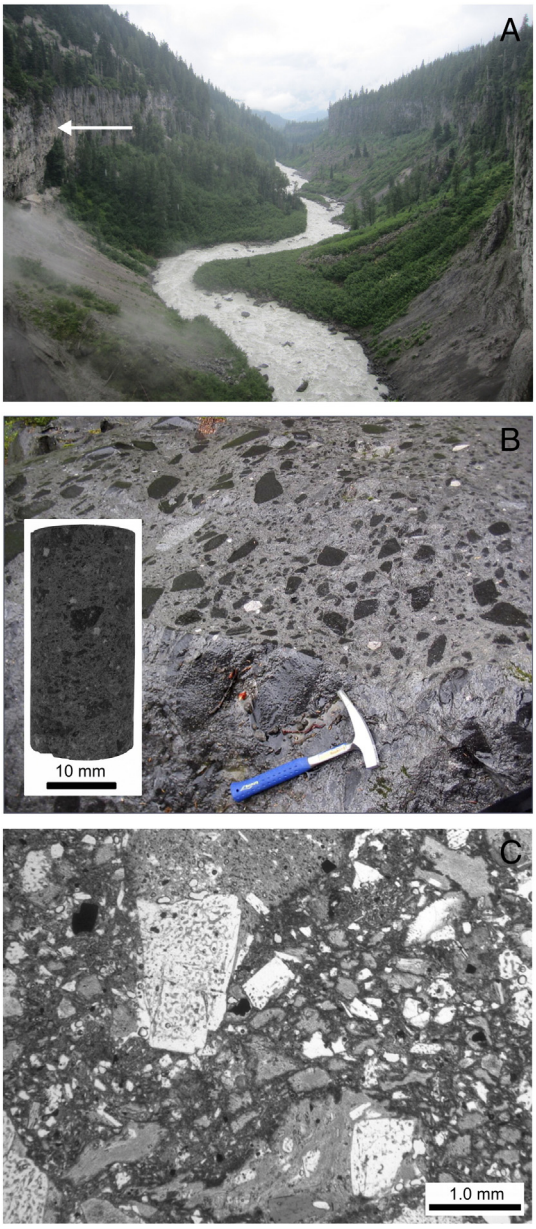

Fig. 1. The natural welded BAF deposit. A: Photograph of the Lillooet River valley taken at Keyhole Falls (photo credit: M. Heap). The welded BAF deposits, forming a 100 m rock wall, are indicated with an arrow. B: Photograph of the welded BAF deposit at Mount Meager volcano (photo credit: K. Michol). Inset shows a cylindrical core sample of the natural deposit (welding Rank IV). C: Photomicrograph of a thin section of the natural deposit (plane-polarized transmitted light).

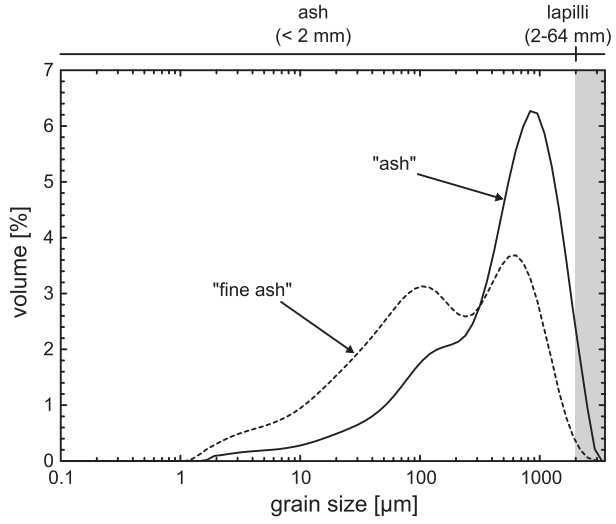

Fig. 2. Laser particle size analysis of aliquots of the fine ash and ash fractions used to create the aggregate samples for our high-temperature compaction experiments.

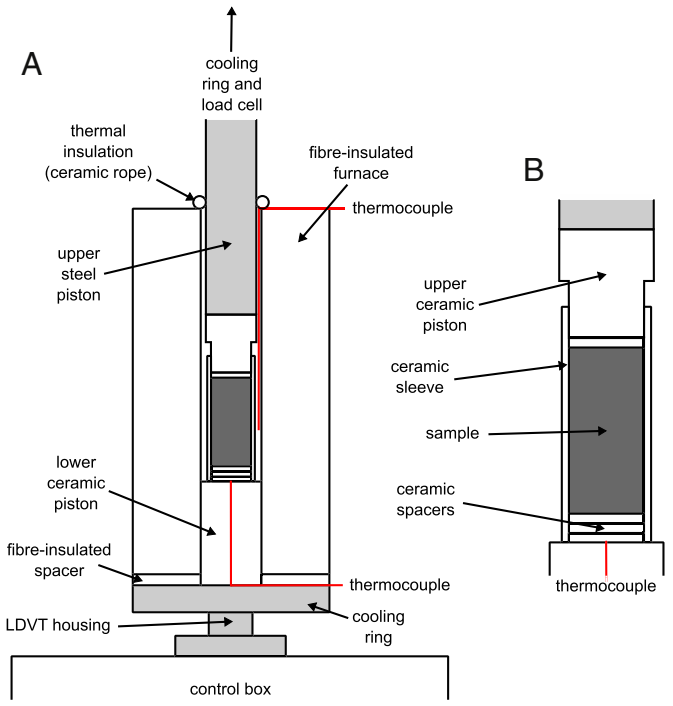

Fig. 3. The experimental setup. A: Schematic diagram of the experimental apparatus at the Volcanology and Petrology Laboratory, Vancouver (not to scale). B: Enlargement of the sample assembly showing the main features (not to scale).

To serve as a comparison, we also collected a suite of variably-welded natural blocks from the BAF deposits at Mount Meager. The welding intensity for the natural blocks, using a scheme similar to that outlined by Quane and Russell (2005), were defined as Rank III (porosity = 30-20%), Rank IV (10-20%), and Rank V (10-5%).

2.2. Methods

Our welding experiments were performed in the high temperature (up to 1100 °C), low load (up to 22.25 kN) Volcanology Deformation Rig (VDR) at the Volcanology and Petrology Laboratory (VPL), University of British Columbia (Quane et al., 2004; Fig. 3). The aggregates were first loaded to a constant stress of 0.03 MPa to ensure that sample packing between the experiments was consistent. The samples were then heated to their target temperatures (800, 850, or 900 °C) at a constant heating rate of 15 °C/min and left to dwell for 1 hour. This dwell time proved to be sufficient for complete thermal equilibration of the sample. We note that, when thermal equilibration was complete, there was a maximum temperature gradient of 3 °C over the whole length of the sample (approximately 88 mm). Our experimental target temperatures span the eruption temperature estimates for the 2360 B.P. eruption (Andrews et al., 2014) and are all above Tg. We then applied a constant stress of 3 MPa, a reasonable estimate of the lithostatic stress at the base of the 160 m thick deposits (Michol et al., 2008). The samples were allowed to deform for 18.5 hours. The samples were then unloaded to 0.03 MPa and cooled back to room temperature at a rate lower than the heating rate (between 5-10 °C/min) to prevent thermal microcracking. We also performed an experiment at room temperature to calibrate the effects of pure mechanical compaction (i.e., non-viscous) of our aggregate. We monitored the load and axial displacement during deformation, from which we calculated the stress (σ), porosity loss, bulk density, axial strain, and axial strain rate ($\dot{\varepsilon}$). The instantaneous viscosity (η_i), the viscosity from the stress and strain rate data evaluated over a specific time interval, was calculated using the following relation:

$$\eta_i = \frac{\sigma}{\dot{\varepsilon}} \quad (1)$$

where $\dot{\varepsilon}$ is the incremental strain rate computed for a time interval of 40 s. All of the experimental products were vacuum saturated with blue epoxy resin and thin sections were prepared for optical microscopic analysis.

Systematic characterisation of rock physical properties (connected and total porosity, density, P-wave velocity, and permeability) was undertaken on cylindrical cores prepared from a suite of variably-welded natural blocks collected at Mount Meager, and on a core sample recovered from the welded material from the 900 °C experiment. Porosity, density, and P-wave velocity were measured on core samples measuring 25.4 mm in diameter with a nominal length of 50 mm. Connected and total porosities were measured using a helium pycnometer and P-wave velocity was measured on dry core samples under a constant uniaxial stress of 0.3 MPa. Steady-state gas permeability was

Table 1
Experimental conditions for the high-temperature compaction experiments, including temperature (RT = room temperature), test duration, axial strain, initial and final total porosity, and initial and final bulk density. Also reported are the instantaneous viscosities (η_i) of the deformed material corresponding to the stable, near-steady-state portion of the experiment (see Fig. 4). All experiments were performed under a constant 3 MPa axial stress.

Temperature, T [°C]	Experiment duration [hours]	Axial strain [%]	Initial total porosity, ϕ^i_T [%]	Final total porosity, ϕ^f_T [%]	Porosity change, $\Delta\phi$ [%]	Initial bulk density [kg/m^3]	Final bulk density [kg/m^3]	Bulk density change [kg/m^3]	Logη_i [Pa s]
900	18.66	18.9	35.8	20.7	-15.1	1600	1980	380	12.7
850	18.68	17.6	34.2	20.0	-14.2	1640	2000	360	13.0
800	18.81	12.3	34.7	25.6	-9.1	1630	1860	230	13.15
RT	18.64	8.7	36.4	30.2	-6.2	1590	1740	150	-

measured on core samples 20 mm in diameter and about 40 mm in length. Permeabilities were measured under a confining pressure of 1 MPa; where applicable the Klinkenberg correction (Klinkenberg, 1941) was applied to our data. The aim of such characterisation was twofold: first, to understand the impact of welding on the rock physical properties and, second, to compare data from natural rocks to our experimental data.

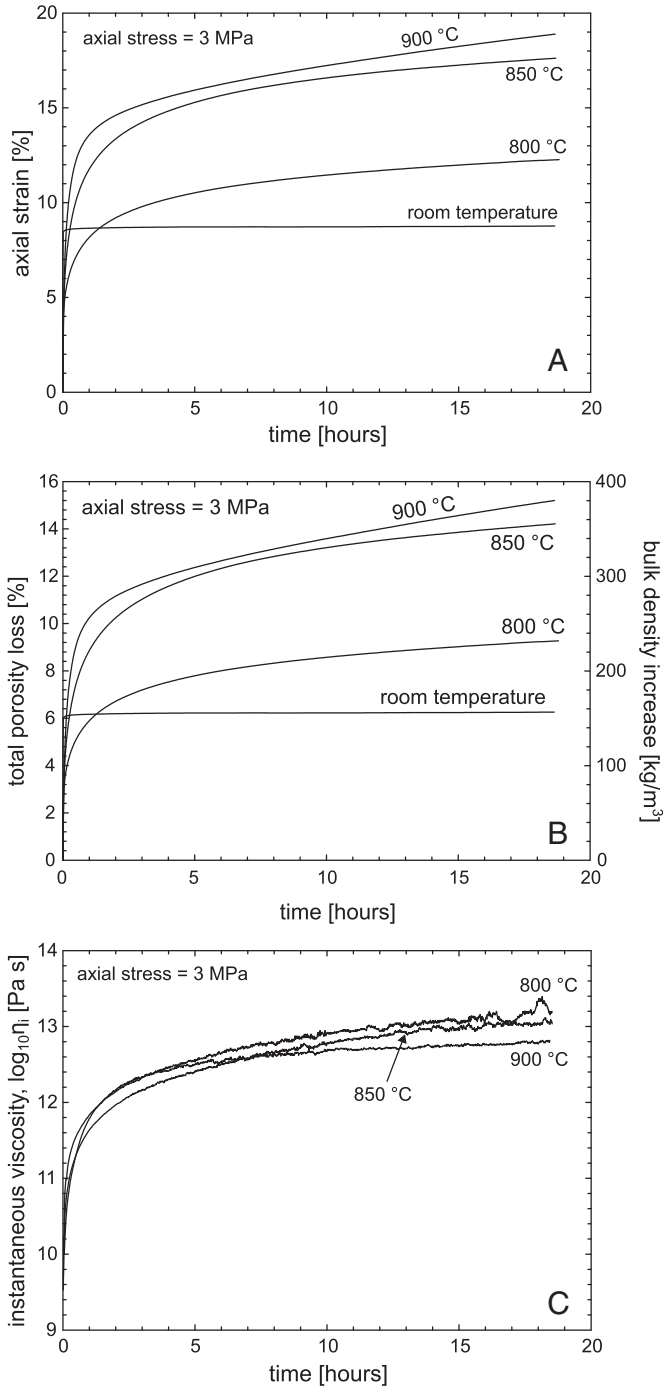

Fig. 4. Data from the high temperature (800-900 °C) and room temperature, constant stress (3 MPa) compaction experiments. Parameters plotted against time include A: Axial strain. B: Total porosity loss and bulk density increase. C: Instantaneous viscosity (calculated using Eq. (1)).

3. Results and discussion

3.1. Welding block-and-ash deposits in the laboratory

The experiments at 800, 850, and 900 °C all showed an initial rapid increase in axial strain, bulk density, and instantaneous viscosity, and an initial rapid decrease in porosity and strain rate (Fig. 4). These rates of change gradually decayed with time, although none of the curves reached a plateau at the end of the experiment. The initial rate of change and the magnitude of the final strain, porosity, and density values were greater as temperature increased. For example, the total axial strain at the end of the experiment was 12.3, 17.6, and 18.9% for the samples at 800, 850, and 900 °C, respectively. At room temperature, following a rapid (30 s) mechanical compaction, the measured properties remained essentially constant for the duration of the experiment. The final values of viscosity recovered from the experiments were generally high ($10^{12.5}$ to 10^{13} Pa s, Fig. 4C) and decreased as temperature increased. The experimental results and conditions are summarised in Table 1.

3.2. The microstructural progression of block-and-ash welding

A summary of our microstructural analysis is provided as Fig. 5. Angular lapilli and ash fragments within a substantial interclast porosity can be seen at room temperature (Fig. 5A). We find some evidence for the sintering of vitric fragments at 800 °C (Fig. 5B). At 850 °C there is a substantial reduction in the interclast porosity (Fig. 5C), a result of the sintering and amalgamation of many vitric fragments. At 900 °C, many of the ash and lapilli fragments have fused together resulting in a dramatic loss of interclast porosity (Fig. 5D). Much of the residual porosity occurs as thin stretched lenses sandwiched between vitric and crystal fragments. We highlight that there is no discernible difference between the sample/microstructure of the natural material (Fig. 1B and C) and the 900 °C experimental product (Fig. 5D, see also Michol et al., 2008).

3.3. The impact of block-and-ash welding on rock physical properties

A summary of the measured physical properties for the natural sample suite, and the 900 °C experimental product, are given in Table 2. Our data show that density and P-wave velocity increase, and that porosity and permeability (Fig. 6) decrease as welding intensifies. If we use porosity and bulk density as proxies for welding, our physical property analysis shows that 900 °C and 850 °C experimental products correspond well to the natural deposit of Rank IV, and our 800 °C experimental product to Rank III (Tables 1 and 2). However, while porosity and density are useful metrics for welding, we argue that permeability holds the greatest potential to highlight whether we have accurately replicated the welding process. This is because permeability captures not only the magnitude of the porosity, but also the connectivity of the porosity. We note that the permeability of the 900 °C sample is very similar to that of the natural Rank IV samples (Table 2 and Fig. 6).

We also observe that, as welding intensity increases, the permeability of the rock approaches that of lava blocks recovered from the BAF deposits. This path represents the return leg of a two-part journey of (1) permeability increase (due to vesiculation and fragmentation) and, (2) permeability decrease (due to welding). On the porosity reduction path, we observe a significant change in the power law exponent of the porosity-permeability data, from about 7.7 above 15% to about 0.5 below 15% (Fig. 6). Our microstructural observations highlight that the change in power law exponent during the return journey could be a result of change in the pore shape and pore space connectivity. The majority of the larger pores and channels are closed at porosities below 15%, leaving only high aspect ratio “crack-like” porosity (e.g., Wright and Cashman, 2013); these features are usually found at the boundaries of viscously unresponsive plagioclase crystals (Fig. 4D). This observation corroborates with the high temperature sintering experiments of Vasseur et al. (2013). The experiments of Vasseur et al.

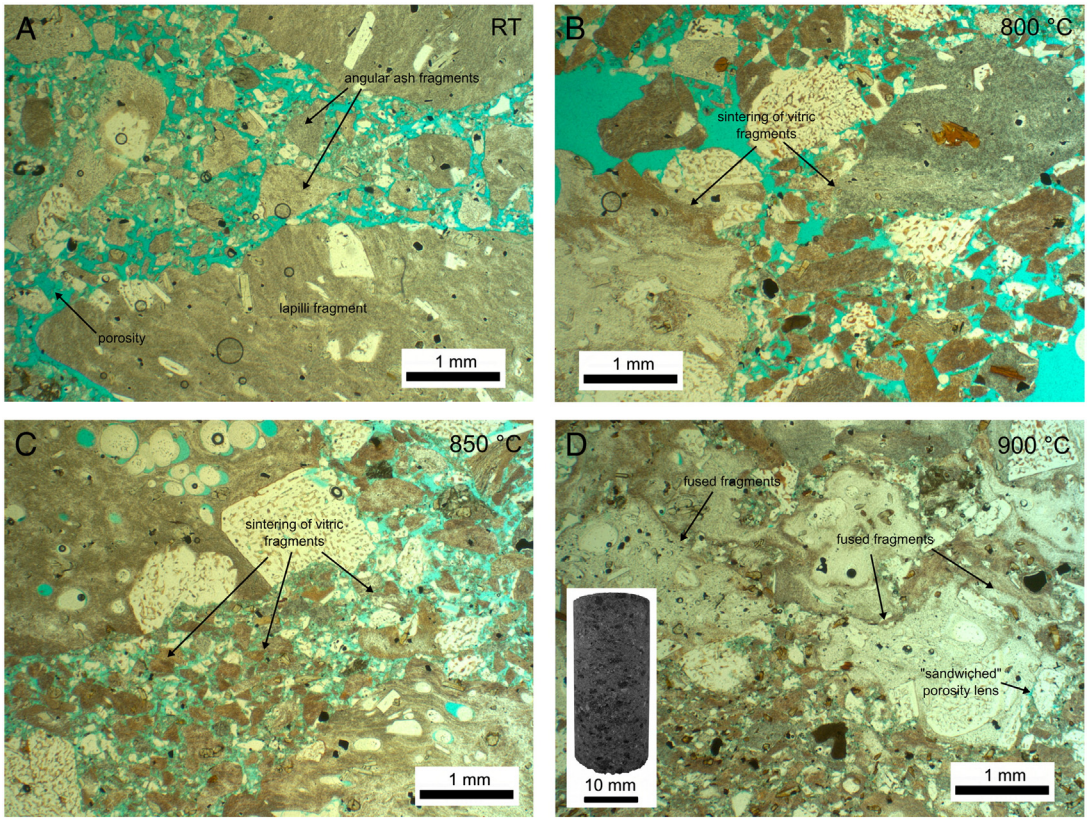

Fig. 5. Photomicrographs (plane-polarized transmitted light) showing the progressive reduction in interclast porosity (the porosity is blue), due to the sintering and amalgamation of vitric fragments, in the experimental aggregate as welding intensity increases. Aggregate compacted at (A) room temperature, (B) 800 °C, (C) 850 °C and, (D) 900 °C. Inset shows a cylindrical core sample of the 900 °C experimental product (welding Rank IV). See text for details.

(2013) showed that, although the total porosity of their sintered glass samples decreased, the isolated porosity increased with sintering time.

The initial increase in permeability (due to vesiculation and fragmentation) is likely to show the opposite trend (as depicted in Fig. 6). For example, permeability data from andesitic dome rocks from Volcán de Colima (Mexico) show that the power law exponent decreases from about 16 below a porosity of 11-14% to about 3 above 15% porosity (Heap et al., 2014). The change to a lower exponent was attributed to a critical vesicle content (a combination of vesicle size and number density) that efficiently connects the microcrack population and allows fluids to travel along a much more direct path through the sample, rather than restricting flow to long and tortuous microcracks (Heap et al., 2014). Therefore, the changes in microstructural pore space connectivity create a pronounced hysteresis in the "*there-and-back-again*" volcanic permeability cycle.

3.4. Welding timescales for block-and-ash flow deposits at Mount Meager

Our high temperature compaction experiments show that welding results in a reduction in porosity and an increase in bulk density and instantaneous viscosity (Fig. 4). To model our data, we have used the following constitutive relationship between the evolving effective viscosity (η_e) and porosity (φ) (Quane and Russell, 2005; Russell and Quane, 2005; Quane et al., 2009; Kolzenburg and Russell, 2014):

$$log\eta_e = log\eta_0 - \frac{\alpha\phi}{1-\phi} \quad (2)$$

where α is an unknown empirical coefficient and η_o is the unknown effective viscosity of the melt plus crystal cargo at zero porosity. While this simple model cannot capture all of the complexity of the experiments over the full deformation path (we do not capture the dynamic behaviour of these experiments at low axial strain; i.e., < 10-15%), we have taken the values of final total porosity (φ^f) and the computed instantaneous viscosity (η_i) from the stable, near steady-state portions of the experiments (Table 1). Values of η_o are temperature dependent and, here, we have assumed an Arrhenian temperature dependence over the range of experimental temperatures (800, 850, and 900 °C). The values of T(K), η_i, and φ^f for our deformation experiments (Table 1) were used to estimate α (using the method described in

Table 2
Rock physical properties of cylindrical cores of natural welded block-and-ash flow deposits, parental lava material, and an experimental product from the high temperature compaction experiment performed at 900 °C. BAF welding rank is determined by porosity. VI = 0-5%; V = 5-10%; IV = 10-20%; III = 20-30%.

	Natural Samples				Post-welding experimental sample (900 °C)
BAF welding rank	V	IV	III	Lava	IV
Bulk density [kg/m^3]	2350	2100	1970	2380	2040
Total porosity, ϕ_t[%]	8.7	19.5	24.7	5.1	18.3
Connected porosity, ϕ_c [%]	7.2	17.5	21.4	4.0	16.5
Gas permeability [m^2]	1.7 x 10^{-15}	5.3 x 10^{-15}	5.9 x 10^{-15}	1.9 x 10^{-15}	2.7 x 10^{-15}
P-wave velocity [km.s^{-1}]	2.80	2.28	2.21	2.79	2.72

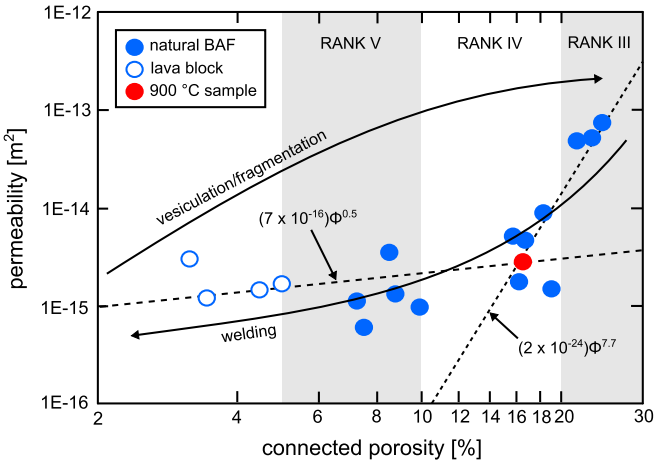

Fig. 6. The impact of welding on the permeability of BAF deposits. Log-log plot of connected porosity versus gas permeability measured for the original lava block, the natural welded BAF deposits, and the 900 °C experimental product. Best-fit power law trends for the low (< 15%) and high (> 15%) porosity samples are also indicted on the figure (the dashed lines). A schematic relationship is shown for permeability evolution resulting from creation (Heap et al., 2014) and the destruction (the data of this study) of porosity, demonstrating the hysteresis of the volcanic permeability cycle. We also show the ranges of porosity we recommend for ranking welding intensity (i.e., III - V) in BAF deposits.

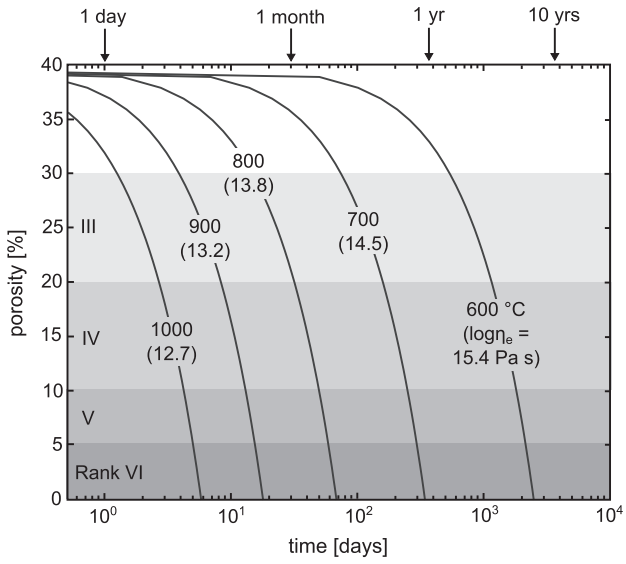

Fig. 7. Rheological model (Eq. (3)) predicting the times required to reduce the porosity of the BAF deposit to 0% as a function of the temperature- (600-1000 °C) dependent effective viscosity (η_e). We modelled for a 160 m ($\sigma \sim 2.4$ MPa) thick pyroclastic deposit that contains an initial porosity of 40% and, thus, a starting density of 1500 kg/m^3. Welding ceases at 0% porosity implying a total volumetric strain of 40%. We also show the ranges of porosity we recommend for ranking welding intensity (i.e., III - VI) in BAF deposits.

Quane et al., 2009). The effective viscosity of the crystal-bearing melt without bubbles (i.e., log η_0 where $\varphi = 0$) can then be determined as a function of temperature, and our α value then used to predict the effective bulk viscosity of the mixture as a function of porosity, and the increase in relative viscosity with decreasing porosity (see also Quane et al., 2009). We note that our value of α (2.0) is higher than the value (0.78) obtained for welding of vitric ash (Quane et al., 2009) and lower than the values obtained for cores of glass beads (5.3; Quane and Russell, 2005) and glass powder (2.4-4; Ducamp and Raj, 1989). The difference in the α value is likely a consequence of differences in sample microstructure (i.e., porosity, crystal content, pore size and shape, particle size and shape, and pore and particle size distribution, amongst others). The model developed here is therefore applicable to the welded BAF deposits at Mount Meager (and other deposits with similar microstructural attributes); drastic differences in microstructure (for example, a difference in volatile content and/or decompression rate is likely to influence the abundance of crystals) will likely require separate estimates for α. Theoretical approaches, such as those described in Mader et al. (2013), may ultimately permit a deeper understanding of the physics buried within the α term. However, our current state of knowledge precludes a purely theoretical approach due to the complex rheological behavior of three-phase (melt, crystals, and bubbles) magmatic/volcanic systems. The results from future experimental studies are expected to guide the development of theoretical models in which the volume fractions and properties of the melt, crystals, and bubbles, and their coupled interactions, are parameterised.

We deploy the rheological model of Russell and Quane (2005) to estimate the timescales for the welding of the BAF deposits at Mount Meager (see also Quane and Russell, 2005; Quane et al., 2009; Kolzenburg and Russell, 2014):

$$\Delta t = \eta_0 \left(\frac{1-\varphi^i}{\alpha\sigma}\right)\left[e^{\left(\frac{-\alpha\varphi}{1-\varphi}\right)} - e^{\left(\frac{-\alpha\varphi^i}{1-\varphi^i}\right)}\right] \quad (3)$$

where σ is the axial stress acting on the deposit and ϕ^i is the initial porosity of the deposit. Our aim was to first capture the behaviour of the Mount Meager case study, and then use the output to prepare a universal model for welding BAF deposits (see next section). The results of the modelling, for a range of effective viscosities, are provided as Fig. 7. For example, at 800 °C, Rank III is achieved after 20 days, Rank IV after 1 month, and Rank V after 50 days. Rank VI deposits were not observed at Mount Meager. These timescales (weeks to months) agree with the inferred time of the collapse of the dam that formed when the BAF deposits accumulated in the Lillooet River valley (Andrews et al., 2014). We also note that, since the dam was breached in under a year, effective viscosities above 10^{15} Pa s do not weld the deposit on a suitable timescale; the modelling therefore suggests that the effective

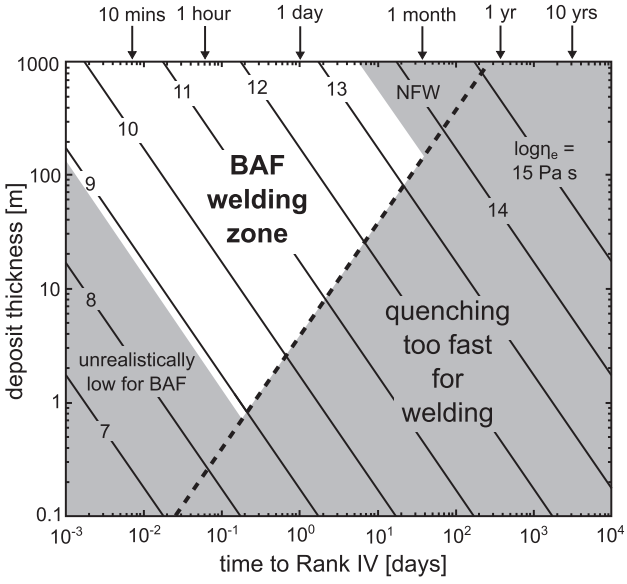

Fig. 8. Universal window (unshaded zone) for the viable welding of BAF deposits, plotted as deposit thickness (m) against the time (days) required to achieve Rank IV welding (see Figs. 6 and 7), and contoured for effective viscosity ($10^{7\text{-}15}$ Pa s). Our diagram highlights three fields where welded BAF deposits will not occur. First, deposits that plot to the right of the dashed black line cool to their glass transition temperatures (i.e., quench) faster than they deform and compact (see text for details). Second, BAF deposits typically derive from processes operating on magmas with viscosities greater than 10^9 Pa s, creating a lower viscosity limit for BAF welding. Third, BAF deposits with very high effective viscosities (i.e., greater than $10^{13.5}$ Pa s) cannot feasibly weld (NFW).

viscosity of the Mount Meager deposit must have been lower than 10^{15} Pa s.

3.5. A universal welding window for block-and-ash flow deposits

Based on our analysis of the Mount Meager case study, we have constructed a universal window for the welding of BAF deposits (Fig. 8) in time-deposit thickness space, contoured for a wide range of effective viscosities. Unlike melt viscosity, the values of effective viscosity (10^7 to 10^{15} Pa s) include all constituents of a multi-phase system, thus accounting for melt composition, water content, temperature, crystallinity, fragment size distributions, and pore size distribution, amongst others. The times given are those required to weld and compact deposits that have an initial porosity of 45% to a porosity of 15% (Rank IV). To accommodate for the suppression of welding due to cooling, we have implemented an "efficient welding cut off", defined as when the centre (x_c) of the deposit falls below 90% of its emplacement temperature (i.e., when $\frac{T_c}{T_e} > 0.9$). We have mapped this boundary (the dashed line on Fig. 8) using a simple conductive cooling model based on the work of Peck et al. (1964):

$$x_c = 2\,(\kappa\, t)^{0.5}\, erfinv\left[\frac{2\,T_c}{T_e} - 1\right] \quad (4)$$

where κ the thermal diffusivity. Although values of κ may vary as a function of porosity, for simplicity we consider a typical value for volcanic deposits of 3.87×10^{-6} m^2/s (see Peck et al., 1964). Below this line we consider that cooling will quench the deposit before Rank IV can be attained. To further constrain our BAF welding window, we consider that (1) an effective viscosity lower than 10^9 Pa s is unrealistically low considering the additional time for cooling and crystallisation for typical BAF source materials and, (2) that deposits with an effective viscosity higher than $10^{13.5}$ Pa s will be too viscous for feasible welding ("NFW" on Fig. 8).

Field studies highlight that BAF deposits commonly have thicknesses less than 10 m (e.g., Boudon et al., 1993). Our BAF welding window suggests deposits with a thickness less than 10 m would require an effective viscosity of less than 10^{11} Pa s to weld. However, due to the inhibiting influence of crystallinity, and the fact that the deposits are usually erupted close to their Tg, perhaps such low viscosities are only achieved in special circumstances. We surmise that high effusion rates and proximal topographic lows will favour the welding of BAF deposits. High effusion rates afford the lavas spawning the BAF events little opportunity to cool below the Tg of their melt phase, and that crystallisation is not complete, prior to collapse. High effusion rates and proximal depressions will both promote rapid deposit accumulation, thereby reducing the time available for cooling the deposit before more material can accumulate. Further, short transport distances reduce the volume of air entrainment by the pyroclastic density current, reducing cooling during transport. Substantial deposit thicknesses, if accumulated rapidly, will thermally insulate the deposit and provide a load to drive viscous deformation at the base of the deposit. The welding of BAF deposits was possible at Mount Meager because the majority of the above criteria were satisfied. The pyroclastic material was channelled into the proximal Lillooet River valley, a deep, narrow valley that runs transverse to the transport direction, via a steep slope beneath the vent (Michol et al., 2008; Andrews et al., 2014). This permitted reduced dispersal, rapid accumulation, and a substantial deposit thickness thus providing limited opportunity for cooling and the load required to drive viscous sintering.

We also highlight that our BAF welding window, and physical property data (e.g., our permeability data), are not necessarily reserved for BAF deposits. Our experiments and modelling could be applied to any volcanic setting containing welded/compacted deposits with a large particle size distribution and a non-insignificant crystal cargo. For example, welded conduit-filling pyroclastic deposits (e.g., Kano et al., 1997; Kolzenburg and Russell, 2014), welded autobreccias in block-lavas and dome lavas of andesitic to rhyolitic composition (e.g., Sparks et al., 1993; Manley, 1996), welding in hot rheomorphic ignimbrite autobreccias (e.g., Branney et al., 1992; Andrews and Branney, 2011), and welding in rhyolitic dykes and conduits (e.g., Tuffen and Dingwell, 2005).

4. Concluding remarks

Welded BAF deposits are rarely observed in nature. As a result, studies on volcanic compaction and welding have been restricted to pumiceous vitric materials. Here, for the first time, we highlight the range of conditions required to weld BAF deposits (and other similar crystal-bearing deposits), guided by high temperature welding experiments, field and microstructural observations, and physical property data collected on a well-described welded BAF. Our study shows that BAF deposits, despite their high crystal cargo (25% in the case of this study), can weld if their melt phase remains above Tg long enough to facilitate sufficient viscous deformation (sintering and amalgamation of vitric fragments). This requires high eruptive fluxes (of material at a temperature above the Tg of its melt phase) and proximal topographical features that allow the deposits to generate significant (i.e., ~ 100 m) insulating thicknesses in a time that precludes significant cooling, and to provide the stress required to drive viscous sintering.

Acknowledgements

We would like to thank Joern Unger and Dave Jones for technical assistance. J. I. Farquharson acknowledges the Initiative D'EXcellence (IDEX) funding framework (Université de Strasbourg). The authors would like to thank Fabian Wadsworth, Heather Wright, and Michael Branney for comments that helped improve this manuscript. We are pleased to acknowledge Graham Andrews and one anonymous reviewer for their constructive comments and suggestions.

References

Abdurachman, E.K., Bourdier, J.-L., Voight, B., 2000. Nuées ardentes of 22 November 1994 at Merapi volcano, Java, Indonesia. J. Volcanol. Geotherm. Res. 100, 345–361.
Andrews, G.D.M., Branney, M.J., 2011. Emplacement and rheomorphic deformation of a large rhyolitic ignimbrite: Grey's Landing, southern Idaho. Bull. Geol. Soc. Am. 123, 725–743. http://dx.doi.org/10.1130/B30167.1.
Andrews, G.D.M., Russell, J.K., Stewart, M.L., 2014. The history and dynamics of a welded pyroclastic dam and its failure. Bull. Volcanol. 76, 811. http://dx.doi.org/10.1007/s00445-00014-00811-00440.
Bachmann, O., Dungan, M.A., Lipman, P.W., 2000. The Pagosa Peak Dacite, San Juan volcanic field, Colorado: Voluminous low-energy eruption prior to a major ash-flow eruption. J. Volcanol. Geotherm. Res. 98, 153–171.
Bierwirth, P. N. (1982), Experimental welding of volcanic ash, Unpubl. B.Sc. Hons. Thesis, Monash University.
Boudon, G., Camus, G., Gourgaud, A., Lajoie, J., 1993. The 1984 nuée-ardente deposits of Merapi volcano, Central Java, Indonesia: Stratigraphy, textural characteristics and transport mechanisms. Bull. Volcanol. 55, 327–342.
Branney, M.J., Kokelaar, B.P., McConnell, B.J., 1992. The Bad Step Tuff: a lava-like rheomorphic ignimbrite in a calc-alkaline piecemeal caldera, English Lake District. Bull. Volcanol. 54, 187–199.
Cas, R.A.F., Wright, J.V., 1987. Volcanic Successions - Modern and Ancient. Unwin Hyman, London (528 p.).
Cole, P.D., Calder, E.S., Sparks, R.S.J., Clarke, A.B., Druitt, T.H., Young, S.R., Herd, R.A., Harford, C.L., Norton, G.E., 2002. Deposits from dome-collapse and fountain-collapse pyroclastic flows at Soufrière Hills Volcano, Montserrat. Geol. Soc. Mem. 21, 231–262.
Ducamp, V.C., Raj, R., 1989. Shear and densification of glass powder compacts. J. Am. Ceram. Soc. 72, 798–804.
Fisher, R.V., Heiken, G., 1982. Mt. Pelée, martinique: may 8 and 20, 1902, pyroclastic flows and surges. J. Volcanol. Geotherm. Res. 13, 339–371.
Friedman, I., Long, W., Smith, R.L., 1963. Viscosity and water content of rhyolite glass. J. Geophys. Res. 68, 6523–6535.
Giordano, D., Russell, J.K., Dingwell, D.B., 2008. Viscosity of magmatic liquids: A model. Earth Planet. Sci. Lett. 271, 123–134.
Grunder, A., Russell, J.K.R., 2005. Welding processes in volcanology: insights from field, experimental, and modeling studies. J. Volcanol. Geotherm. Res. 142, 1–9.
Grunder, A., Laporte, D., Druitt, T.H., 2005. Experimental and textural investigation of welding: effects of compaction, sintering vapor-phase crystallization in the rhyolitic Rattlesnake Tuff. J. Volcanol. Geotherm. Res. 142, 89–104.
Guest, J.E., Rogers, P.S., 1967. The sintering of glass and its relationship to welding in ignimbrites. Proc. Geol. Soc. Lond. 1641, 174–177.

Heap, M.J., Lavallée, Y., Petrakova, L., Baud, P., Reuschlé, T., Varley, N., Dingwell, D.B., 2014. Microstructural controls on the physical and mechanical properties of edifice-forming andesites at Volcán de Colima, Mexico. J. Geophys. Res. 119, 2925–2963.

Hickson, C.J., Russell, J.K., Stasiuk, M.V., 1999. Volcanology of the 2350 B.P. Eruption of Mount Meager Volcanic Complex, British Columbia, Canada: implications for Hazards from Eruptions in Topographically Complex Terrain. Bull. Volcanol. 60, 489–507.

Kano, K., Matsuura, H., Yamauchi, S., 1997. Miocene rhyolitic welded tuff infilling a funnel-shaped eruption conduit Shiotani, southeast of Matsue, SW Japan. Bull. Volcanol. 59, 125–135.

Kerr, P.F., Gavesci, A.T., Bowes, D.R., 1974. Welded glass-breccias from Marysvale, Utah. Geol. Mag. 111, 15–22.

Klinkenberg, L.J., 1941. The permeability of porous media to liquids and gases. Drill. Prod. Pract. 200–213.

Kolzenburg, S., Russell, J.K., 2014. Welding of pyroclastic conduit infill: A mechanism for cyclical explosive eruptions. J. Geophys. Res. 119, 5305–5323.

Mader, H.M., Llewellin, E.W., Mueller, S.P., 2013. The rheology of two-phase magmas: A review and analysis. J. Volcanol. Geotherm. Res. 257, 135–158.

Manley, C.R., 1996. In situ formation of welded tuff-like textures in the carapace of a voluminous silicic lava flow, Owyhee County, SW Idaho. Bull. Volcanol. 57, 672–686.

Michol, K.A., Russell, J.K.R., Andrews, G.D.M., 2008. Welded block and ash flow deposits from Mount Meager, British Columbia, Canada. J. Volcanol. Geotherm. Res. 169, 121–144.

Peck, D.L., Moore, L.G., Kojima, G., 1964. Temperatures in the crust and melt of the Alae lava lake, Hawaii, after the August 1963 eruption of Kilauea volcano. A preliminary report., *U.S. Geol. Survey Prof. Paper 501D*, pp. D1–D7.

Quane, S.L., Russell, J.K.R., 2005. Welding: insights from high-temperature analogue experiments. J. Volcanol. Geotherm. Res. 142, 67–87.

Quane, S.L., Russell, J.K.R., Kennedy, L., 2004. A low-load, high-temperature deformation apparatus for volcanological studies. Am. Mineral. 89, 873–877.

Quane, S.L., Russell, J.K., Friedlander, E.A., 2009. Time scales of compaction in volcanic systems. Geology 37, 471–474.

Rodríguez-Elizarrarás, S., Siebe, C., Komorowski, J.C., Espíndola, J.M., Saucedo, R., 1991. Field observations of pristine block- and ash-flow deposits emplaced April 16-17, 1991 at Volcán de Colima, Mexico. J. Volcanol. Geotherm. Res. 48, 399–412.

Rodríguez-Losada, J.A., Hernández-Gutiérrez, L.E., Lomoschitz Mora-Figueroa, A., 2007. Geotechnical features of the welded ignimbrites of the Canary Islands. In: Malheiro, A.M., Nunes, J.C. (Eds.), Volcanic rocks - proceedings of ISRM Workshop W2, Ponta Delgada, Azores, Portugal, 14–15 July, 2007. Taylor & Francis Group, London.

Russell, J.K., Quane, S.L., 2005. Rheology of welding: inversion of field constraints. J. Volcanol. Geotherm. Res. 142, 173–191.

Ryan, A., Russell, J.K., Nichols, A.R.L., Hess, K.-U., 2014. Experiments and models on H2O retrograde solubility in volcanic systems, in revision.

Sparks, R.S.J., Stasiuk, M.V., Gardeweg, M., Swanson, D.A., 1993. Welded breccias in andesite lavas. J. Geol. Soc. 150, 897–902.

Sparks, R.S.J., Tait, S.R., Yanev, Y., 1999. Dense welding caused by volatile resorption. J. Geol. Soc. 156, 217–225.

Stewart, M.L., 2002. Dacite block and ash avalanche hazards in mountainous terrains: 2360 yr. Master of Science thesis,BP eruption of Mount Meager, British Columbia. University of British Columbia.

Tuffen, H., Dingwell, D.B., 2005. Fault textures in volcanic conduits: evidence for seismic trigger mechanisms during silicic eruptions. Bull. Volcanol. 67, 370–387.

Ui, T., Matsuwo, N., Sumita, M., Fujinawa, A., 1999. Generation of block and ash flows during the 1990–1995 eruption of Unzen Volcano, Japan. J. Volcanol. Geotherm. Res. 89, 123–137.

Vasseur, J., Wadsworth, F.B., Lavallée, Y., Hess, K.-U., Dingwell, D.B., 2013. Volcanic sintering: Timescales of viscous densification and strength recovery. Geophys. Res. Lett. 40, 5658–5664.

Wright, H.M.N., Cashman, K.V., 2013. Compaction and gas loss in welded pyroclastic deposits: evolution of porosity and permeability in the Shevlin Park Tuff. Geol. Soc. Am. Bull. http://dx.doi.org/10.1130/B30668.30661.

Yasui, M., Koyaguchi, T., 2004. Sequence and eruptive style of the 1783 eruption of Asama Volcano, central Japan: a case study of an andesitic explosive eruption generating fountain-fed lava flow, pumice fall, scoria flow and forming a cone. Bull. Volcanol. 66, 243–262.